THE ASTROPHYSICAL JOURNAL, 476:649–665, 1997 February 20

SIMULATED VLBI IMAGES FROM RELATIVISTIC HYDRODYNAMIC JET MODELS

AMY J. MIODUSZEWSKI[1] AND PHILIP A. HUGHES
Department of Astronomy, University of Michigan, 834 Dennison, Ann Arbor, MI 48109-1090; amy@astro.lsa.umich.edu

AND

G. COMER DUNCAN
Department of Physics and Astronomy, Bowling Green State University, Bowling Green, OH 43403
Received 1996 June 3; accepted 1996 September 16

ABSTRACT

A series of simulated maps showing the appearance in total intensity of flows computed using a recently developed relativistic hydrodynamic code (Duncan & Hughes) are presented. The radiation transfer calculations were performed by assuming that the flow is permeated by a magnetic field and fast particle distribution in energy equipartition, with energy density proportional to the hydrodynamic energy density (i.e., pressure). We find that relativistic flows subject to strong perturbations exhibit a density structure consisting of a series of nested bow shocks, and that this structure is evident in the intensity maps for large viewing angles. However, for viewing angles less than 30°, differential Doppler boosting leads to a series of knots of emission that lie along the jet axis, similar to the pattern exhibited by many VLBI sources. The appearance of VLBI knots is determined primarily by the Doppler boosting of parts of a more extended flow. To study the evolution of a perturbed jet, a time series of maps was produced, and an integrated flux density light curve created. The light curve shows features characteristic of a radio-loud AGN: small-amplitude variations and a large outburst. We find that in the absence of perturbations, jets with a modest Lorentz factor (~ 5) exhibit complex intensity maps, while faster jets (Lorentz factor ~ 10) are largely featureless. We also study the appearance of kiloparsec jet-counterjet pairs by producing simulated maps at relatively large viewing angles; we conclude that observed hot spot emission is more likely to be associated with the Mach disk than with the outer bow shock.

Subject headings: galaxies: jets — hydrodynamics — methods: numerical — shock waves

1. INTRODUCTION

Most radio-loud active galactic nuclei (AGNs), when mapped using very long baseline interferometry (VLBI), show a stationary core and knots of emission that sometimes move superluminally. These features are believed to be the most prominent parts of a jet of relativistic plasma (Blandford & Königl 1979; Lind & Blandford 1985), and the superluminal motion and general absence of a counterjet leave little doubt that relativistic effects (Doppler shift, Doppler boosting, aberration, time delays, etc.) play a crucial role in determining the appearance of these flows. The recent development of relativistic hydrodynamic codes has greatly enhanced our ability to explore the dynamics of such extragalactic jets. However, a comparison of the simulated flow with single-dish and VLBI data requires the computation of a radiated flux density—ideally, the Stokes parameters I, Q, and U—from the flow. Since the relativistic effects influencing the appearance of AGNs are strongly dependent on the viewing angle, it is important to compute simulated images for a jet aligned at various angles to the line of sight. In some earlier studies, this has been done by using nonrelativistic hydrodynamics to simulate the conditions inside the jet and relativistic formulae to compute the radiation flux density. For example, Wilson & Scheuer (1983) study the appearance of kiloparsec-scale structures by assuming that no relativistic particles (i.e., synchrotron emission) are present except in the shock front. With the advent of relativistic hydrodynamical codes, a consistent calculation of the radiation field is possible that allows one to properly include relativistic effects in both dynamics and radiation transfer.

Since the radiated flux density is determined by the magnetic field intensity and fast particle distributions, which are not computed in the hydrodynamic simulations, some assumptions must be made about how those quantities are related to the hydrodynamic variables. Our assumptions about these quantities (namely, that the magnetic field intensity and particle distributions are proportional to the hydrodynamical pressure) are very similar to those adopted in nonrelativistic or steady state relativistic simulations (e.g., Rayburn 1977; Williams & Gull 1984; Wilson 1987). Jun, Clark, & Norman (1994) have studied cosmic-ray–mediated magnetohydrodynamical shocks using a two-fluid approach; such a consistent computation of the magnetic field intensity and radiating particle distributions is highly desirable, but is currently beyond the scope of studies that aim to elucidate the overall flow dynamics of relativistic jets. In this paper, we present the first results from a study that adopts a simple mapping between hydrodynamic and high-energy species, and that highlights the very different morphologies exhibited by the flow material and by the associated radiation flux density. Gómez et al. (1995) employ a similar procedure but concentrate on what effect varying the density profile of the confining medium has on the appearance of the jet. In § 2, the relativistic hydrodynamical code used to produce the data is summarized. Section 3 describes the radiation transfer calculations. We discuss the simulated maps and the integrated flux density light curve in § 4. Conclusions and future work are presented in § 5.

2. RELATIVISTIC COMPUTATIONAL FLUID DYNAMICS

We use a method for the numerical solution of the Euler equations that has been found to be both robust and effi-

[1] Current address: NRAO, P.O. Box O, Socorro, NM 87801.

cient, and that permits treatment of relativistic flows. The evolved variables are mass, momentum, and total energy density, in the *laboratory* frame. With the adoption of these quantities, the relativistic Euler equations have a form identical to that of the nonrelativistic equations, thus allowing a direct application of techniques devised for the latter. Our approach employs a solver of the Godunov-type, with approximate solution of the local Riemann problems. In this method, the RHLLE technique, a relativistic generalization of a method developed originally for nonrelativistic fluids (Harten, Lax, & van Leer 1983; Einfeldt 1988), the full solution to the Riemann problem is approximated by two discontinuities separating a constant state, whose value must satisfy the Euler equations in conservation form. However, velocity and pressure appear explicitly in the relativistic Euler equations, in addition to the evolved variables, and pressure and rest density are needed for the computation of the wave speeds that form the basis of the numerical technique. We obtain these values by performing a Lorentz transformation at every time and cell boundary (or center) where the rest-frame values are required. The Lorentz transformation involves a numerical root finder to solve a quartet equation for the velocity. This provides robustness because it is straightforward to ensure that the computed velocity is always less than the speed of light. The relativistic Euler equations and Lorentz transformation are described in Appendix A.

We achieve second-order accuracy in time by computing fluxes at the half-time step. The Godunov method requires a "reconstruction" step, in which cell-centered values of variables in juxtaposed cells are used to estimate the cell boundary values of these quantities. It is this linear interpolation that provides second-order spatial accuracy. However, it is possible for the rest-frame quantities corresponding to the interpolated laboratory frame values to be unphysical, corresponding to a velocity in excess of the speed of light, and/or negative pressure. Such behavior is easily trapped, and our scheme (rarely) falls back locally to first-order if needed.

The solver is implemented in a two-dimensional axisymmetric form within the framework of an adaptive mesh refinement (AMR) algorithm (Quirk 1991), allowing us to perform high-resolution, two-dimensional simulations with modest computing resources. The AMR is used to ensure that the grid density is locally adequate for an accurate rendition of sharp features, such as shocks, while admitting computations on workstation-class machines of modest speed and memory. In this approach, the solution is stored in a hierarchy of "patches," each of which is a logically rectangular grid, with a number of patches at each level of the hierarchy. In regions of little activity, a coarse grid is sufficient, and the solution is known on a set of abutting domains with cell size equal to that adopted for the unrefined grid. In regions where significant structure lies, the solution must be taken from patches of higher cell density, embedded within the coarsest mesh. One must either interpolate the values of the state variables to a uniform mesh with scale equal to that of the finest refined mesh (with consequent increase in needed storage) or, when performing the radiation transfer calculations discussed herein, compute the locations of intersection between a line of sight and the boundaries that describe the hierarchy of patches. The latter is particularly difficult to implement when time delay effects are to be considered, because the data populating the cells used for radiation transfer will be epoch-dependent at each point along a ray, but the patch structure changes with epoch. We are currently building a radiation transfer code that can accommodate time delays without losing the benefits of the Adaptive Mesh structure. For the radiation transfer calculations described here, we interpolate onto a single fine mesh and do not account for light-travel–time effects. Combinations of various Lorentz factors ($1 < \gamma < 10$), Mach numbers ($6 < \mathscr{M} < 15$), and adiabatic indices ($\Gamma = 4/3$ or $\Gamma = 5/3$) were studied by Duncan & Hughes (1994), where some further details of both the solver and the AMR are presented, together with the first results from this code.

3. RADIATION TRANSFER CALCULATIONS

For the radiation transfer calculation, the potentially complex mesh structure associated with AMR is circumvented by first interpolating the hydrodynamic data onto a single fine rectangular mesh, which represents a cut through the axis of the axially symmetric flow. The scale of this mesh is chosen to equal that of the most refined patches employed in the hydrodynamic simulation. A Lorentz transformation of the values determined by the hydrodynamic simulation then provides the pressure and the axial and radial components of velocity in each cell of this mesh. The rectangular data set may be rotated through 360° to populate a cylindrical volume with three-dimensional data. To facilitate the radiation transfer calculations, a three-dimensional rectangular coordinate system is established, so that the "observer's" lines of sight are in planes parallel to one side of the mesh. This mesh is populated with data by reference to the original, fine, two-dimensional data set, having computed the axial and radial coordinates corresponding to the cell location in three dimensions. The radial component of velocity is decomposed into two Cartesian components, thus providing each cell with a value for pressure and three components of velocity. For a given viewing angle, lines of sight are projected through the mesh. For each intersected mesh cell, the hydrodynamic pressure and velocities are extracted from the three-dimensional data set. Then, for each line of sight, starting at the far side of the mesh and stepping along the line of sight, these values are used in radiation transfer calculations to determine the flux density at the surface of the mesh. The mesh scale can be coarsened for a "quick look" at the data set or used at a scale similar to that of the data. The viewing angle, optical depth, spectral index, and frequency are free parameters in a given radiation transfer computation. With no coarsening, the mesh is 1000 by 320 by 320 cells for the cases explored here. We define the jet radius as 160 uncoarsened grid cells.

A primary goal of this study is to examine the distribution of synchrotron flux density; thus, values for the synchrotron emissivity and opacity must be computed. The synchrotron emissivity (j_ν) and opacity (κ_ν) depend upon the high-energy particle distribution (n_0), the magnetic field intensity (B), the frequency (ν), and the spectral index (α). In the reference frame of the plasma (Pacholczyk 1970),

$$j_\nu \propto n_0 B^{\alpha+1} \nu^{-\alpha} , \tag{1}$$

$$\kappa_\nu \propto n_0 B^{\alpha+3/2} \nu^{-(\alpha+5/2)} . \tag{2}$$

Assuming minimum energy, which approximates energy equipartition, it follows that the radiating particle number density, n_0, and the magnetic field energy density, u_B, are directly proportional to the hydrodynamical pressure (p), i.e., the internal energy density, u_e. If

$$u_B = u_e , \tag{3}$$

and

$$p = (\Gamma - 1)u_e , \tag{4}$$

where Γ is the adiabatic index, then $u_B \propto p$ and $u_e \propto p$. Therefore, since the magnetic field energy density is

$$u_B = \frac{B^2}{2\mu_0} , \tag{5}$$

then

$$B \propto p^{1/2} . \tag{6}$$

The high-energy particle energy density is given by

$$u_e = \int_{E_L}^{E_H} n_0 E^{-\delta} E\, dE , \tag{7}$$

where E_H and E_L are the high and low particle energy cutoffs, respectively, and δ is the slope of the particle energy spectrum ($=2\alpha + 1$). If $E_H \gg E_L$ and $\delta > 2$, then

$$u_e \simeq \frac{n_0 E_L^{-\delta+2}}{\delta - 2} , \tag{8}$$

so that

$$n_0 \propto p , \tag{9}$$

if E_L is a constant or slowly varying function of position and time.

So, substituting equations (6) and (9) into equations (1) and (2), we find

$$j_\nu \propto p^{(\alpha+3)/2} \nu^{-\alpha} , \tag{10}$$

$$\kappa_\nu \propto p^{(2\alpha+7)/2} \nu^{-(\alpha+5/2)} . \tag{11}$$

Equations (10) and (11) describe the dependency of the radiation transfer coefficients on pressure, but some normalization must be adopted. The normalization of the emissivity is arbitrary, since the underlying hydrodynamic calculations were independent of length scale and an arbitrary choice of length scale would lead to an arbitrary intensity for an optically thin flow. The normalization of opacity is chosen to provide the adopted optical depth (which is a free input parameter) for a line of sight with a typical path length through the flow at the given angle of view. An average value of the minimum and maximum pressures ($\langle p \rangle$) over the whole computational domain is used in computing the normalization.

Adopting $\nu = 1$ as a fiducial frequency, and with L the total path length through the flow as just described, for a desired optical depth τ,

$$\kappa_\nu = \frac{\tau}{L} \left(\frac{p}{\langle p \rangle} \right)^{(2\alpha+7)/4} \nu^{-(\alpha+5/2)} . \tag{12}$$

The actual optical depths for different lines of sight deviate from τ, but this approach provides a method of tuning the optical depth to explore the appearance of optically thin and thick flows, through a single parameter that may be set prior to performing the radiation transfer calculations.

Synchrotron radiation transfer calculations for the total intensity, I, are performed following Rybicki & Lightman (1979), allowing for Doppler boost and frequency shift. Generally, the laboratory frame spectral intensity, I, is equal to $\mathscr{D}^3$ times the rest-frame spectral intensity, where $\mathscr{D} = [\gamma(1 - \beta \cos \theta)]^{-1}$ is the Doppler factor for a flow speed βc and angle of view θ. However, as we discuss below, the pattern of structures evident in the flows under study changes slowly, and we can approximate the flow as a fixed distribution of relativistic velocities within a stationary "window" in the observer's frame. Thus (Cawthorne 1991),

$$I = I_0 e^{-l\kappa_\nu} + \frac{j_\nu}{\kappa_\nu} \mathscr{D}^2 (1 - e^{-l\kappa_\nu}) , \tag{13}$$

where β is the velocity normalized to the speed of light (v/c), $\gamma = (1 - \beta^2)^{-1/2}$, and l is the line of sight thickness of an individual cell. We have used $\alpha = 0.75$ throughout the computations reported therein.

The magnetic field is assumed to be tangled with length scale much less than that of a computational cell. Therefore, since, for the simulations reported here, there is no preferred field direction within a cell, aberration does not change the average effective field orientation and may be ignored. Ideally, for a full treatment of relativistic effects, light-travel–time effects should be included. Light-travel–time effects complicate the radiation transfer because hydrodynamic data must be available for all times along the evolution of the jet. Komissarov & Falle (1996) overcome this by incorporating time delay radiation transfer into their relativistic hydrodynamic code as it runs. Here time delay effects have been ignored because, although the maximum instantaneous flow speeds are relativistic, the jet *structures* move at barely relativistic speeds: we observe $\beta_{\text{shock}} \simeq 0.59$ for the slowest relativistic case and $\beta_{\text{shock}} = 0.89$ for the fastest relativistic case studied here. This is a consequence of the large-amplitude variations in inflow Lorentz factor for the perturbed case: the shocks driven by these variations are strong and so move rapidly forward in the frame of the upstream fluid; weak shocks would move at close to the fluid speed and thus move rapidly in the observer's frame. In fact, the exclusion of such delay effects does not affect our conclusions, which depend on the significant differential Doppler boosting between the flow close to the axis and the flow far from the axis, not on placement of structures along the flow axis.

4. MAPS AND ANALYSIS

Figure 1 contains schlieren-type images that show the *gradient* of the laboratory frame density from the hydrodynamical simulations used to produce the images shown in Figures 2, 3, 4, 5, and 6. The first four cases are from Duncan & Hughes (1994). The first three have Lorentz factors ~ 1, 5, and 10, respectively, and adiabatic index 5/3; the fourth has Lorentz factor 10 and adiabatic index 4/3. The fifth case has the same parameters as the fourth, but the inflow Lorentz factor was sinusoidally modulated between ~ 1 and 10 to induce perturbations. Figures 2–6 present the results of the radiation transfer calculations for these five hydrodynamic simulations at four viewing angles (θ): 10°, 30°, 60°, and 90°. The four panels are logarithmically scaled contour maps produced by the radiation transfer program at the four viewing angles. The peak flux density differs from map to map and is proportional to the Doppler boost, except in the nonrelativistic case (Fig. 2). Note that the maps are dominated by the head/bow region, and while the

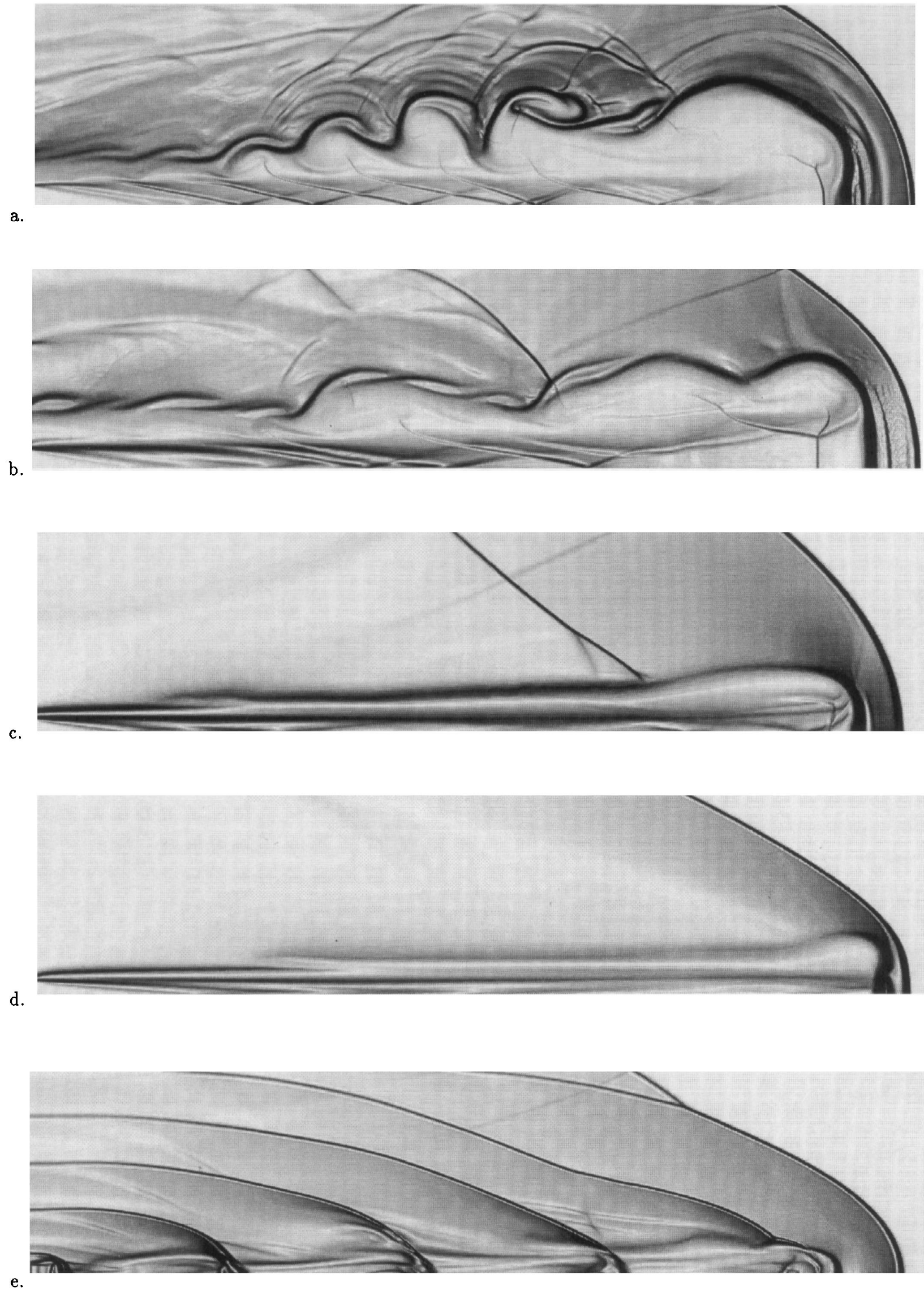

FIG. 1.—Schlieren-type images of laboratory frame density gradient with (*a*) $\beta = 0.3$ and $\Gamma = 5/3$; (*b*) $\gamma = 5$ and $\Gamma = 5/3$; (*c*) $\gamma = 10$ and $\Gamma = 5/3$; (*d*) $\gamma = 10$ and $\Gamma = 4/3$; and (*e*) same as (*d*), but with inflow Lorentz factor modulated between 1 and 10 to induce perturbations.

incident-reflection shock pattern remains visible in the nonrelativistic case, in general, there is little internal jet structure evident. The dynamic range of these maps is similar to a low (20:1) dynamic range VLBI map.

The hydrodynamic simulation of the perturbed jet exhibits a series of nested bow shocks, which are also evident in the simulated maps (Fig. 6) for angles of 90° and 60°; however, when the viewing angle is decreased to less than 60°, the pattern of emission takes the form of *knots along the axis*. To explore this effect, Figure 7 presents a calculation of the emissivity ($j \propto p^{(\alpha+3)/2}$) for a slice of the middle of the jet, and the Doppler boosting ($\mathscr{B} \propto \mathscr{D}^{2+\alpha}$) that would exist at four angles of view in a slice through the center of the perturbed jet. Figure 7*a* shows that rest-frame emissivity is enhanced primarily at the bow shocks. Figures 7*b* and 7*c* demonstrate that, at small viewing angles, the Doppler boosting accentuates the core of the flow, while at larger viewing angles, Doppler boosting has little effect on the appearance of the jet. Comparing the distinctive signature of emissivity and Doppler boosting shown in Figure 7 with the morphology of the maps shown in Figure 6 strongly suggests that, at small viewing angles, the image mor-

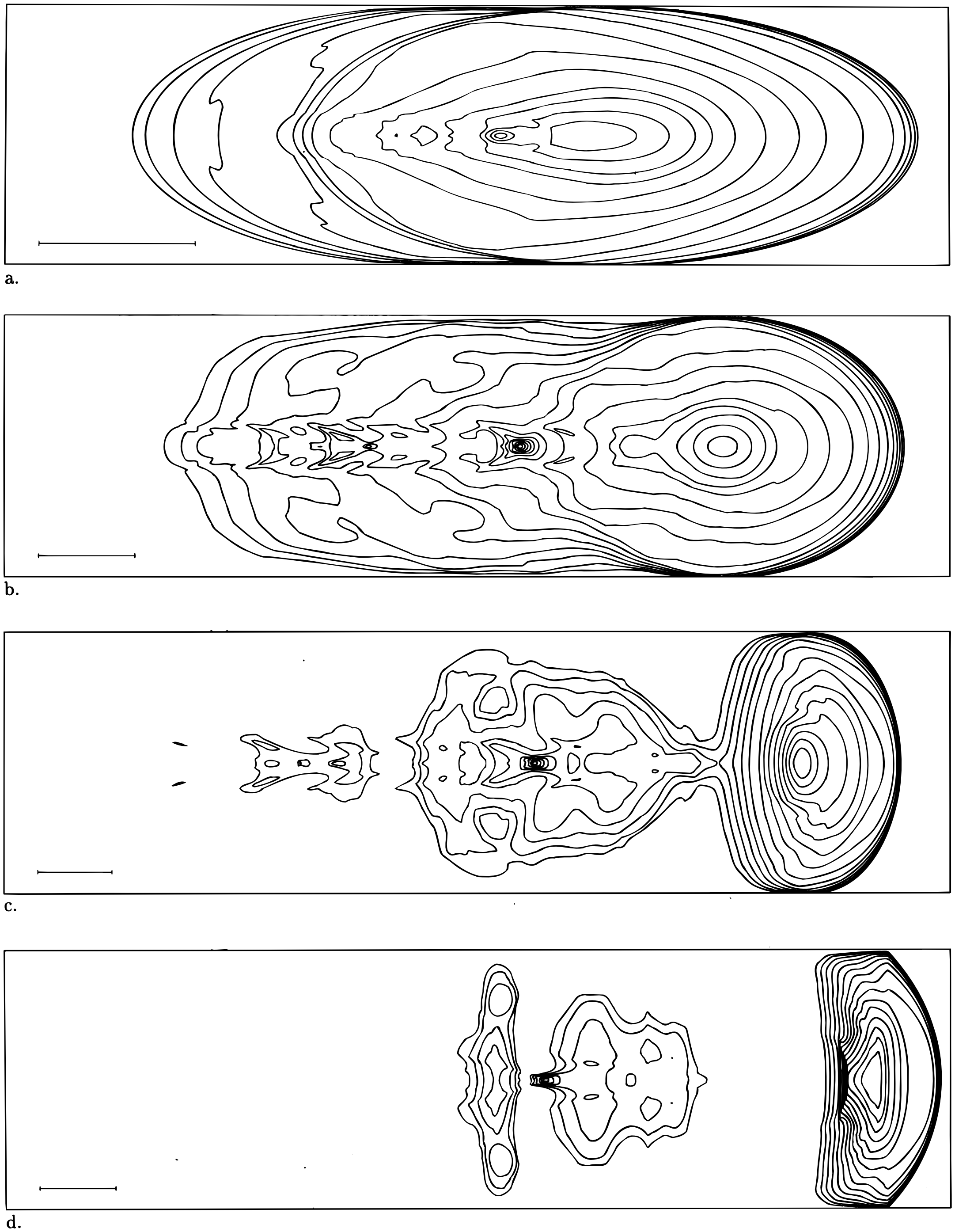

FIG. 2.—Flux maps from the simulation shown in Fig. 1*a*. $\bar{\mathscr{I}}_{\rm max}$ is the maximum flux density in the map normalized to the maximum flux density in the 10° map [$\mathscr{I}_{\rm max}(10°) = 0.04773$] at the following viewing angles: (*a*) $\theta = 10°$, $\bar{\mathscr{I}}_{\rm max} = 1.0$ (*b*) $\theta = 30°$, $\bar{\mathscr{I}}_{\rm max} = 0.7310$; (*c*) $\theta = 60°$, $\bar{\mathscr{I}}_{\rm max} = 0.9382$; and (*d*) $\theta = 90°$, $\bar{\mathscr{I}}_{\rm max} = 1.191$. The contour levels are 5%, 6.11%, 7.45%, 9.10%, 11.12%, 13.57%, 16.57%, 20.24%, 24.71%, 30.17%, 36.84%, 44.98%, 54.93%, 67.07%, and 81.90% of $\mathscr{I}_{\rm max}$. The bar in the lower left-hand corner of each map represents a length of $\frac{1}{2}$ jet radii.

phology is determined primarily by the Doppler boosting of the high-velocity jet, whereas at larger angles, the intrinsic emissivity is more important.

To examine where the transition in viewing angle from "bow shock–dominated" to "jet flow–dominated" flow occurs, a simple measure of the local flux density contribution ($\mathscr{B}j$) was calculated for a patch near the jet axis and a patch off-axis containing bow shock structure, as a function of viewing angle. The results of this calculation, shown in Figure 8, demonstrate that the angle at which transition from "bow shock–dominated" to "jet flow–dominated" occurs is $\sim 20°$. This issue may also be addressed analytically (see Appendix B), by relating emissivity to pressure, pressure to the velocity jump at the bow shock, and determining at what angle of view Doppler boosting of the jet flow produces an intensity that exceeds that associated with the bow a few jet radii off-axis. This approach leads to a similar conclusion, namely, that the jet should dominate for viewing angles less than $\sim 30°$. These results are somewhat at odds with the result from visual inspection of the maps, which indicates that the transition is somewhere between 30° and 60°. The explanation for this lies in the fact that

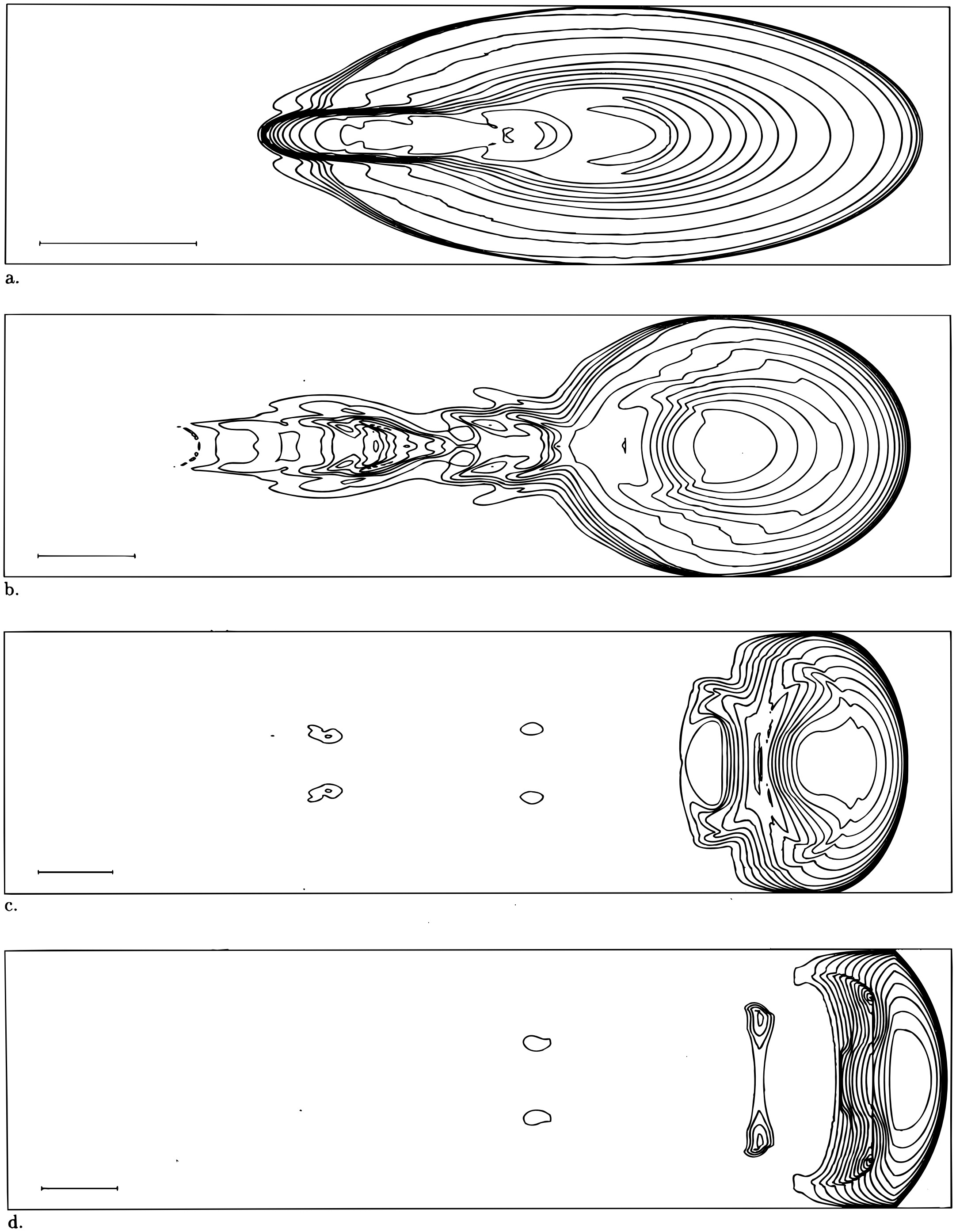

FIG. 3.—Flux maps from the simulation shown in Fig. 1*b*. $\bar{\mathscr{F}}_{\rm max}$ is the maximum flux density in the map normalized to the maximum flux density in the 10° map [$\mathscr{F}_{\rm max}(10°) = 1.833 \times 10^3$] at the followng viewing angles: (*a*) $\theta = 10°$, $\bar{\mathscr{F}}_{\rm max} = 1.0$; (*b*) $\theta = 30°$, $\bar{\mathscr{F}}_{\rm max} = 0.6028$; (*c*) $\theta = 60°$, $\bar{\mathscr{F}}_{\rm max} = 0.3918$; and (*d*) $\theta = 90°$, $\bar{\mathscr{F}}_{\rm max} = 0.3693$. The contour levels are the same as those used in Fig. 2. The bar in the lower left-hand corner of each map represents a length of $\frac{1}{2}$ jet radii.

neither calculation takes line-of-sight effects into account. The regions of high Doppler boosting are "thick" (~ 120 pixels wide), as opposed to the regions of high emissivity, which are long and "thin" (only ~ 15 pixels wide). Therefore, at large viewing angles, a line of sight will travel through more cells of high emissivity than at small angles. The exact opposite would be true for the regions of high Doppler boosting. Taking this into account, the local flux density contribution as a function of viewing angle was calculated by summing along a line of sight through two patches, one containing an off-axis bow shock and the other containing a region of high Doppler boosting near the axis, both approximately 120 pixels wide. The line of sight, for the patch containing the bow shock, was selected so that it would intersect the bow shock for all angles of view. These calculations indicate a transition angle of $\sim 50°$ (see Fig. 9), which is much more consistent with what is shown in the maps.

For the perturbed case, maps were generated using output of the hydrodynamical data every 150 computational cycles, to create 26 time slices of the perturbed jet. The intensities were summed for each map, and a light

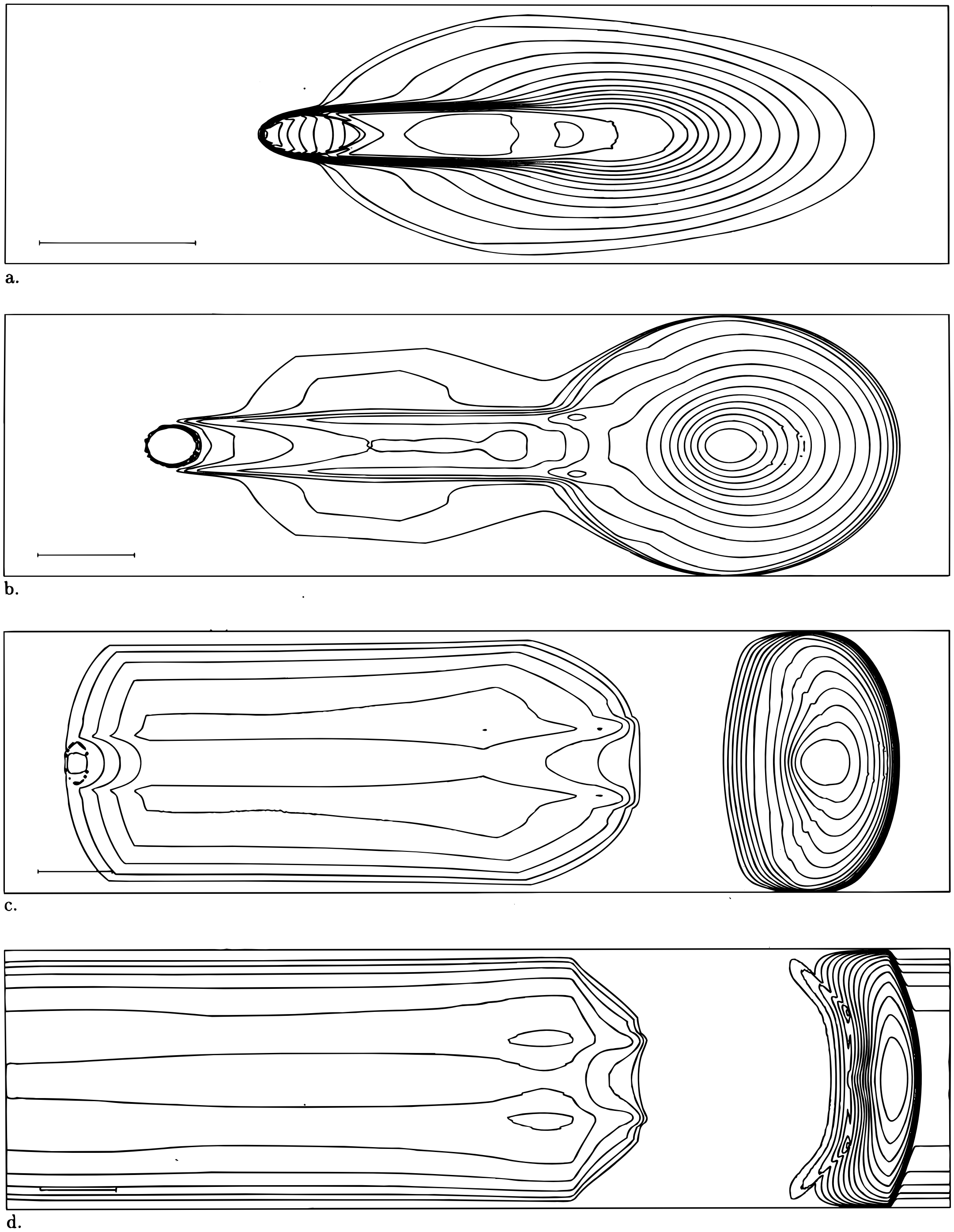

FIG. 4.—Flux maps from the simulation shown in Fig. 1*c*. $\bar{\mathscr{I}}_{max}$ is the maximum flux density in the map normalized to the maximum flux density in the 10° map [$\mathscr{I}_{max}(10°) = 3.977 \times 10^5$] at the followng viewing angles: (*a*) $\theta = 10°$, $\bar{\mathscr{I}}_{max} = 1.0$; (*b*) $\theta = 30°$, $\bar{\mathscr{I}}_{max} = 0.2690$; (*c*) $\theta = 60°$, $\bar{\mathscr{I}}_{max} = 0.09952$; and (*d*) $\theta = 90°$, $\bar{\mathscr{I}}_{max} = 0.7913$. The contour levels are the same as those used in Fig. 2. The bar in the lower left-hand corner of each map represents a length of $\frac{1}{2}$ jet radii.

curve such as would result from single-dish monitoring was created at three different frequencies. These light curves are shown in Figure 10 for a viewing angle of 30°; the "central" frequency (ν in Fig. 10) is the frequency used in previously discussed simulations. The simulated light curves are indeed suggestive of some of the large-amplitude outbursts displaying substructure and a constant flux density level, seen in the University of Michigan Radio Astronomy Observatory (UMRAO) database (Aller et al. 1985). An example of this is shown in Figure 11, where, beginning in 1988, UMRAO observed an outburst in the BL Lac object 0735+178 (H. D. Aller & M. F. Aller 1995, private communication). As in the simulated light curve, there are low-amplitude fluctuations as well as a large-amplitude outburst. The variations were examined in detail by calculating the emissivity and Doppler boosting along the jet axis for all time slices. This shows that the lower amplitude total flux density variations are indeed a result of the onset of shocks. Of course, these simulations cannot be expected to reproduce many of the features seen in single-dish monitoring data, which are generally accepted to arise from the passage of shocks into an optically thin portion of a diverg-

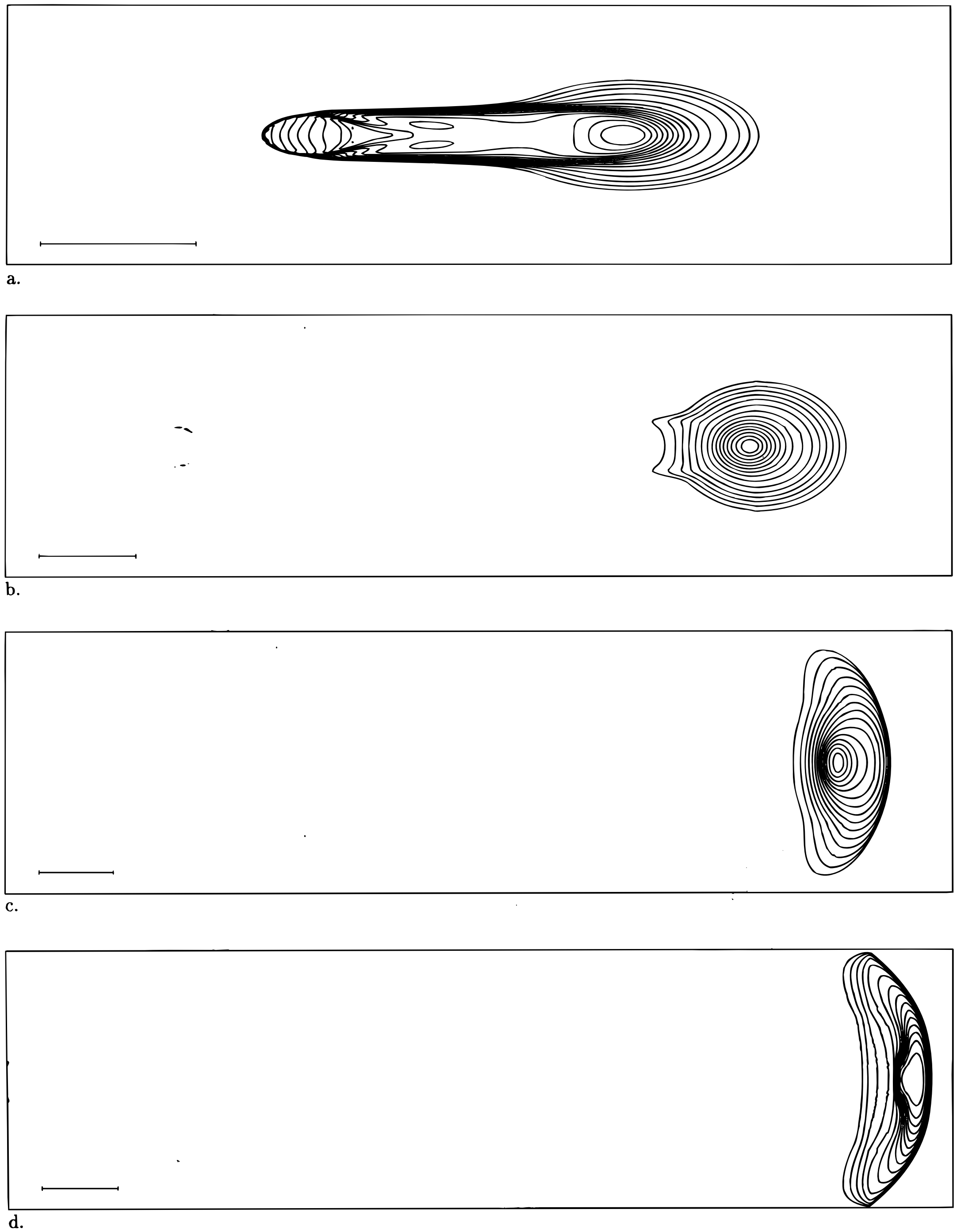

FIG. 5.—Flux maps from the simulation shown in Fig. 1*d*. $\bar{\mathcal{I}}_{\rm max}$ is the maximum flux density in the map normalized to the maximum flux density in the 10° map [$\mathcal{I}_{\rm max}(10°) = 3.678 \times 10^6$] at the followng viewing angles: (*a*) $\theta = 10°$, $\bar{\mathcal{I}}_{\rm max} = 1.0$; (*b*) $\theta = 30°$, $\bar{\mathcal{I}}_{\rm max} = 0.3619$; (*c*) $\theta = 60°$, $\bar{\mathcal{I}}_{\rm max} = 0.09742$; and (*d*) $\theta = 90°$, $\bar{\mathcal{I}}_{\rm max} = 0.04538$. The contour levels are the same as those used in Fig. 2. The bar in the lower left-hand corner of each map represents a length of $\frac{1}{2}$ jet radii.

ing flow, with subsequent adiabatic energy loss, because the hydrodynamic models employed here have neither a diverging inflow nor an ambient pressure gradient, and so they undergo no significant lateral expansion.

A further similarity to the monitoring data is the damping of the variations at the lowest frequency. The nature of the variations seen in the lowest flux density curve ($\nu/3$ in Fig. 10) is explained by the fact that this is near the spectral turnover between the optically thin and the optically thick parts of the spectrum, and opacity effects are masking the contributions from far portions of the flow: we see only the longish timescale fluctuations of structures near the $\tau = 1$ surface, rather than the sum of the weakly correlated variations from the whole body of the emitting volume. In contrast, the structure in the higher frequency light curves is caused both by the creation of new components at the inflow and by the overtaking of a component by another component. A striking feature of the light curves is that there is very little evidence for periodicity, which is surprising given that the perturbations were driven using a sinusoidal modulation of the inflow Lorentz factor. To ascertain whether a Fourier analysis could pick out period-

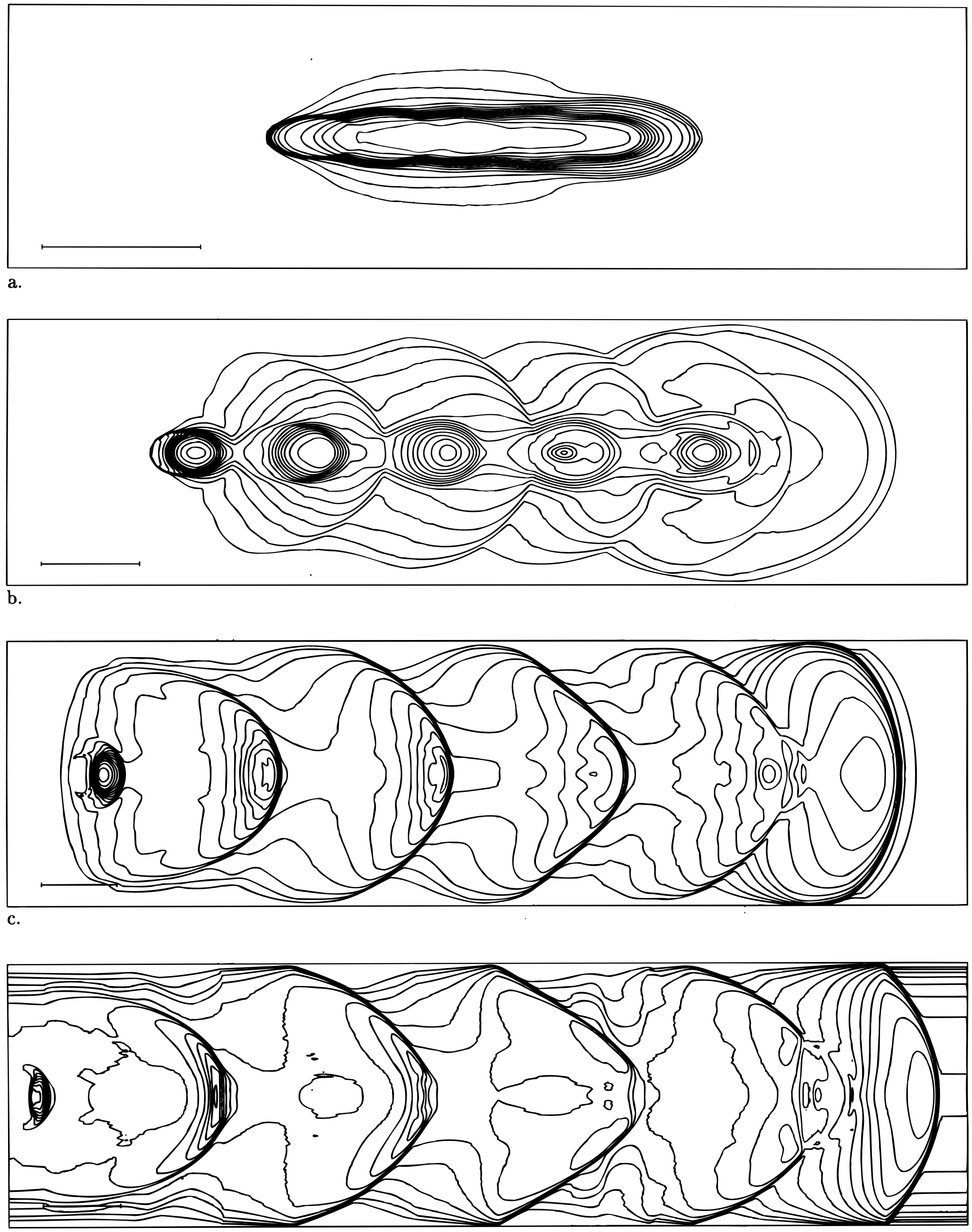

FIG. 6.—Flux maps from the simulation shown in Fig. 1*e*. $\bar{\mathscr{I}}_{max}$ is the maximum flux density in the map normalized to the maximum flux density in the 10° map [$\mathscr{I}_{max}(10°) = 8.050 \times 10^5$] at the followng viewing angles: (*a*) $\theta = 10°$, $\bar{\mathscr{I}}_{max} = 1.0$; (*b*) $\theta = 30°$, $\bar{\mathscr{I}}_{max} = 0.2211$; (*c*) $\theta = 60°$, $\bar{\mathscr{I}}_{max} = 0.07793$; and (*d*) $\theta = 90°$, $\bar{\mathscr{I}}_{max} = 0.04716$. The contour levels are the same as those used in Fig. 2. The bar in the lower left-hand corner of each map represents a length of $\frac{1}{2}$ jet radii.

icity where the eye could not, we constructed a Scargle periodogram (Scargle 1982), shown in Figure 12. (Scargle provides a "false alarm probability," which aids in judging the significance of peaks in the power distribution.) No periodicity is evident, there being only the broad distribution of power associated with the large-amplitude rise seen in the light curves. Evidently, such a feature, occurring within a time series with limited sampling of only a few cycles of the modulation, masks the signature of the latter. This may be a warning that, in order to see clear evidence of periodicity, it is necessary to have a well-sampled data set spanning many cycles of activity that sustain the same frequency of variation. Indeed, the character of radio wave band variability can change significantly over a timescale of years, and there is little evidence from such data sets for periodicity (Aller, Aller, & Hughes 1996).

Figure 13 shows simulated maps corresponding to the 11th–14th time slices, which cover the time interval of the large outburst seen in the light curve. Notice that in Figure 13*a* and 13*b*, the second component overtakes the first component, and a fourth knot is formed. Also note that the components in these maps move away from the core—

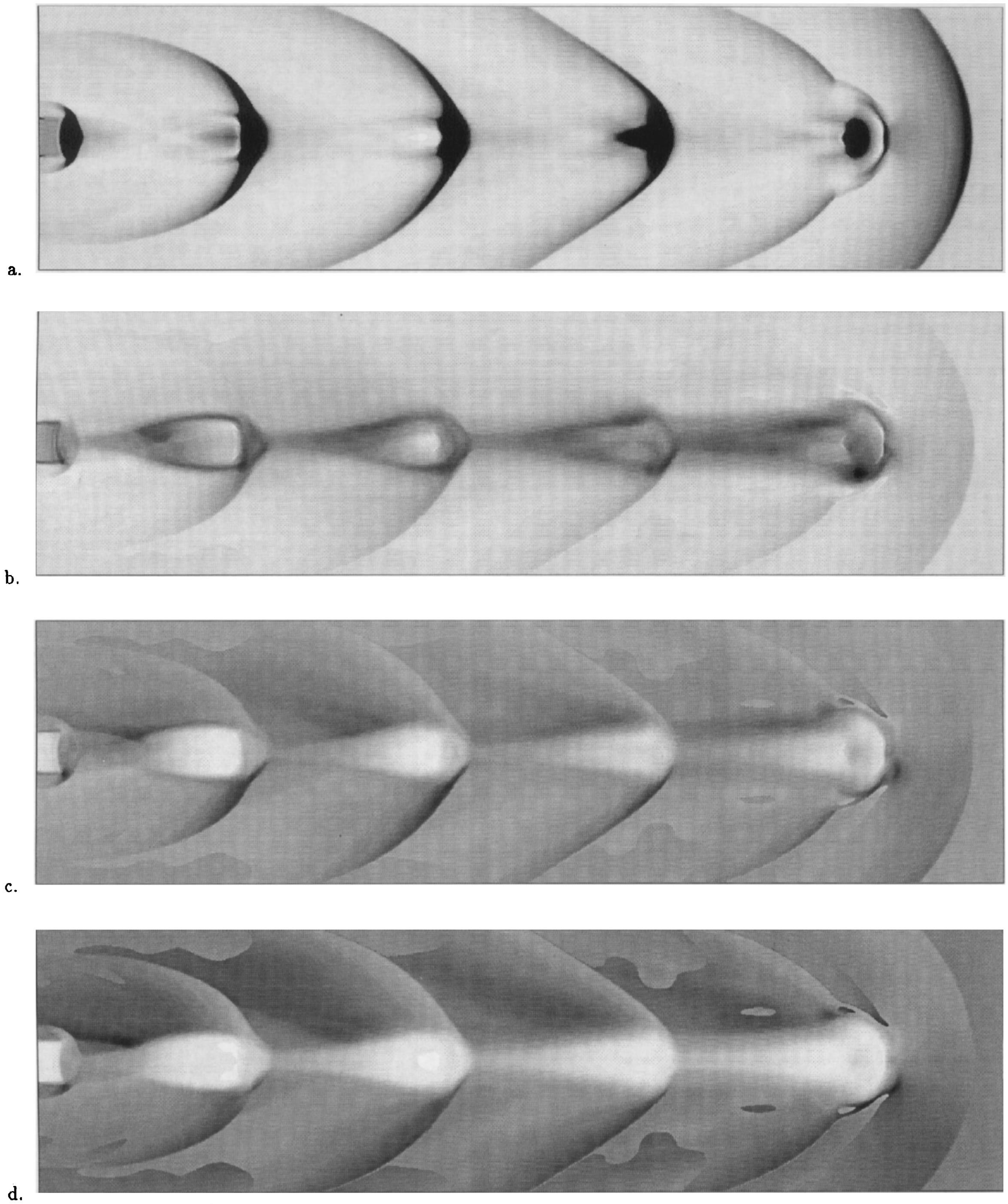

FIG. 7.—Linear gray-scale plots, where a darker color means a higher intensity, of (*a*) the emissivity ($p^{1.875}$); $\mathscr{I}_{\max} = 1.110 \times 10^5$; the Doppler boosting ($\mathscr{D}^{2.75}$) at (*b*) $\theta = 30°$, $\mathscr{I}_{\max} = 13.46$; (*c*) $\theta = 60°$, $\mathscr{I}_{\max} = 4.126$; and (*d*) $\theta = 90°$, $\mathscr{I}_{\max} = 2.447$ of a slice through the perturbed jet.

behavior very similar to that seen in many multiepoch VLBI maps (e.g., Zensus & Pearson 1990). Figure 14 shows the motion of each component over time. The position of each component was determined by recording the position of the peak flux density. The components move at about the same speed, the average component velocity being 0.14 jet radii/time step with a standard deviation of 0.033 jet radii/time step. Also notice the apparent acceleration in component 3 between time steps 20 and 21. Component 3 is double peaked, and between time steps 20 and 21, the maximum flux density in the component moves from the rearmost peak to the forward-most peak, causing this apparent acceleration. This would suggest that component accelerations in observed jets might be associated with a continuous and simple change in the distribution of emitting material, rather than acceleration of plasma or a change in shock propagation speed. It must be noted that we have not seen merging (or overtaking of components) produce motion against the flow.

A plot of the flux densities of the individual components as they move along the jet is shown in Figure 15. Most components show similar flux density histories as they evolve. However, the first and "combined" components show dramatic deviation from this behavior. The flux density increase in the combined component dominates the outburst shown in the light curve. An examination of the component flux densities versus time shows that the outburst arises from the fact that the combined component has

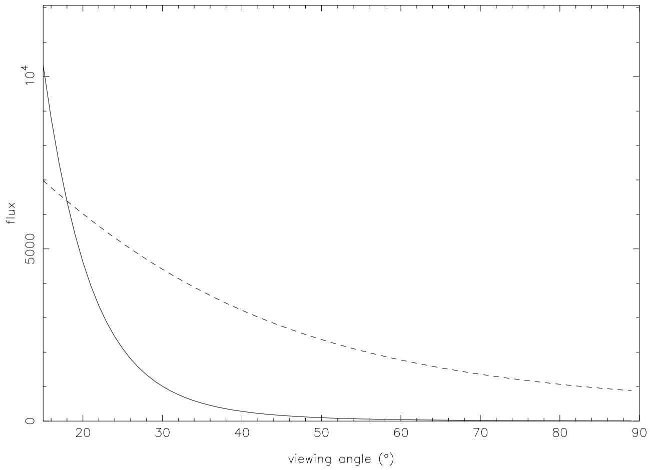

FIG. 8.—Plot of the flux density (arbitrary units) vs. angle for a region of high Doppler boosting (*solid line*) and a region of the same size of high emissivity offset one-third of a jet radii from the flow (*dashed line*) for a slice through the jet.

~2.5 times the flux density as the summed flux densities of components 1 and 2 in the previous time slice. Inspection of the hydrodynamic variables shows that this outburst results from a dramatic increase in the hydrodynamical pressure when a shock overtakes another shock—the dramatic rise in flux density is a direct consequence of hydrodynamical effects, not of, for example, a change in Doppler boosting associated with a change in flow speed.

5. KILOPARSEC-SCALE STRUCTURES

Although we have focused on the "VLBI-like" structure, it is important to note that the hydrodynamic simulations are scale-free and therefore can be applied to the study of kiloparsec-scale jets. There has long been a debate about the origin of the emission from the "hot spot and nearby lobe" structure seen in many FR II radio galaxies (Bridle & Perley 1984). The emission from the hot spot and its environment could originate from an internal shock (the Mach disk), from the more extended bow shock, or from both structures. Recall that we assume emissivity is depen-

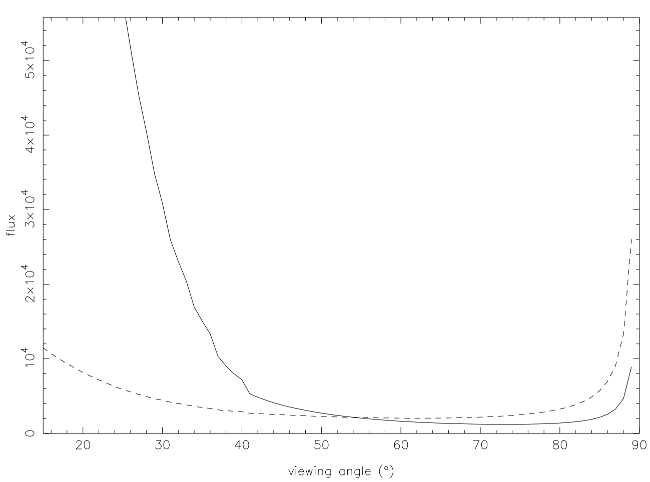

FIG. 9.—Plot of flux density (arbitrary units) vs. angle summed for a line of sight through a region of high Doppler boosting (*solid line*) and a line of sight through a region of the same size of high emissivity offset from the central axis (*dashed line*).

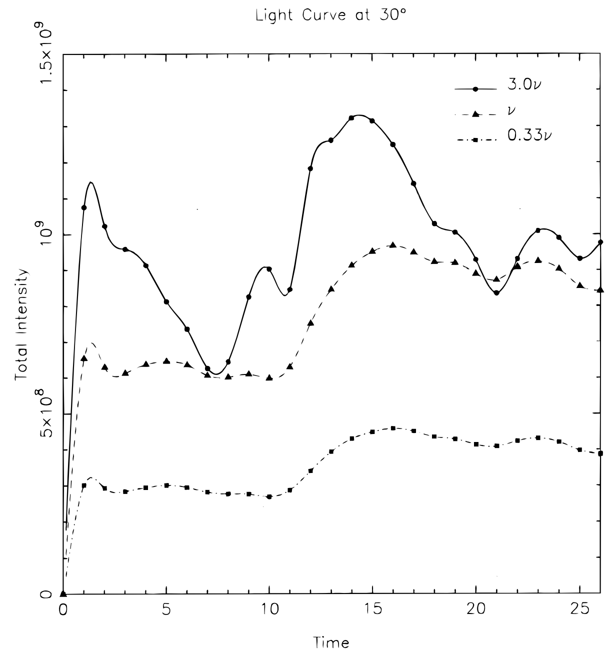

FIG. 10.—Light curve at 30° of the time-evolved perturbed jet

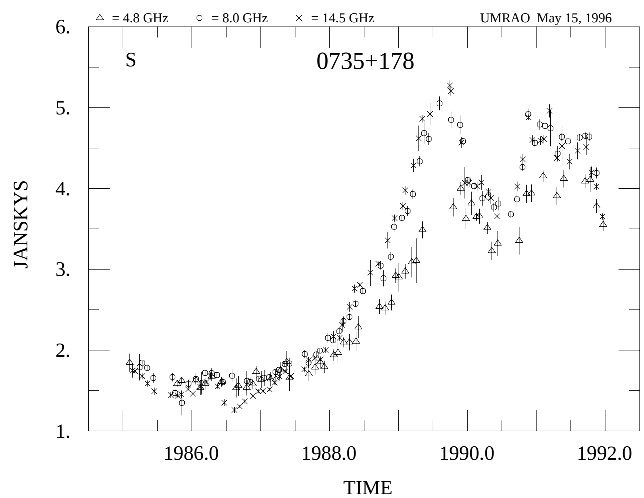

FIG. 11.—Light curve of BL Lac object 0735+178 from the UMRAO database.

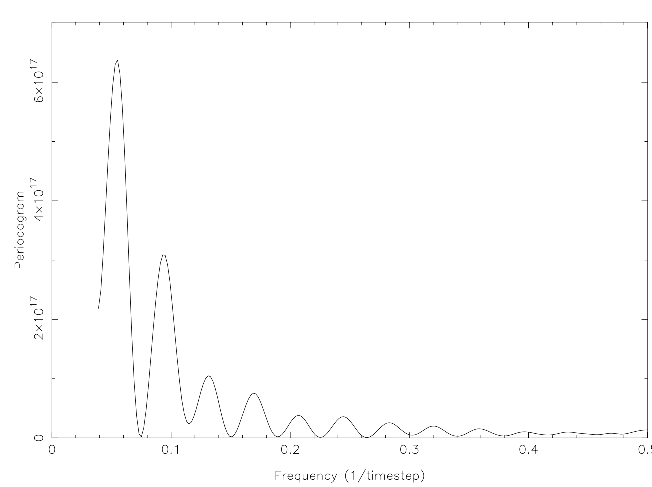

FIG. 12.—The periodogram analysis of the central light curve shown in Fig. 10.

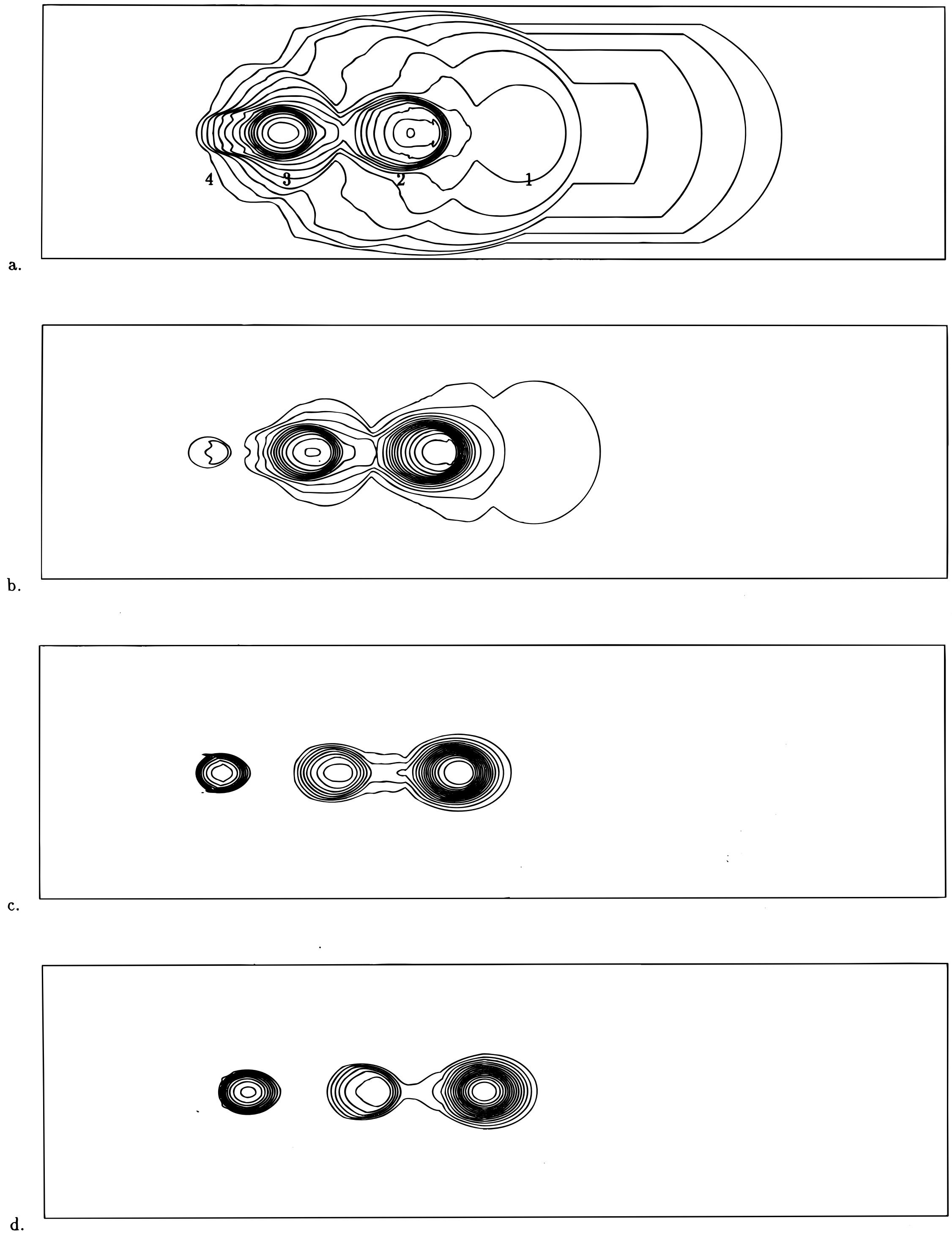

FIG. 13.—Flux maps of the (*a*) 11th, (*b*) 12th, (*c*) 13th, and (*d*) 14th time slice of the evolving perturbed jet; $\mathscr{I}_{\max} = 1.560 \times 10^5$. The contour levels are the same as those used in Fig. 2.

dent only on pressure, i.e., particle acceleration is not included in our modeling. The distribution of pressure maxima and minima in the vicinity of the Mach disk–bow shock region—and thus the distribution of rest-frame emissivity—will not be the same as the distribution of particles accelerated by, for example, the first-order Fermi process at either the Mach disk or the bow shock. If the emission is determined by the latter, then maps produced using the techniques discussed above, although providing a valid indication of the likely general distribution of intensity, will not be right in detail. With that caveat in mind, we now ask how the intensity distribution correlates with flow structures at the head of the source.

Figure 16 shows maps of two-sided jets with intermediate viewing angles (45°, 60°, and 75°) using the $\gamma = 10$ simulation (see Fig. 1*d* and Fig. 5). The jet that is approaching is on the right, while the corresponding receding jet is on the left. Notice that the maps in Figure 16 show a hot spot and nearby lobe structure, the latter becoming more prominent with an increase of viewing angle. Also, as the viewing angle

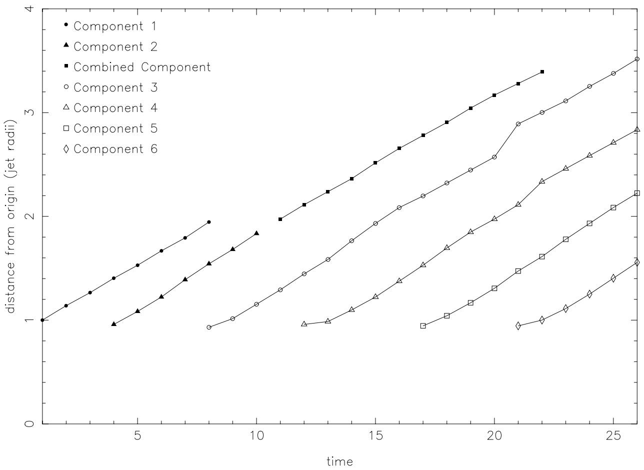

FIG. 14.—Component velocities; the position of each component vs. time.

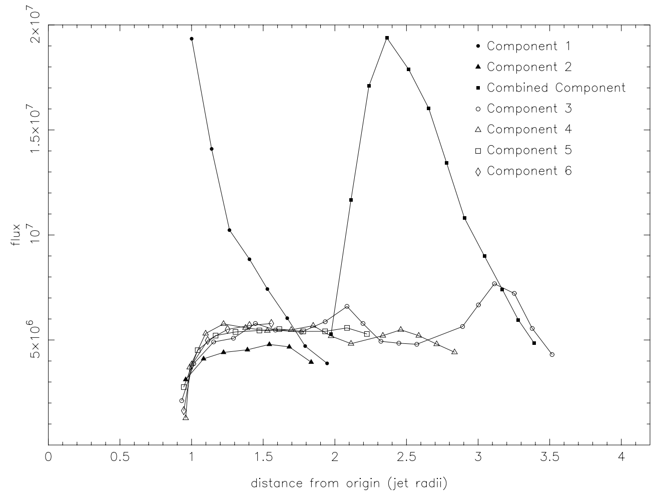

FIG. 15.—Component flux density evolution; flux vs. how far the component has traveled along the jet.

increases, the opposing jet becomes stronger, and a lobe structure develops there as well. The brightness ratios between the pairs of jets are 19.4, 6.9, and 2.5 for the 45°, 60°, and 75° jet pairs, respectively. Bridle & Perley (1984) defined "one-sided" jets as those with a brightness ratio of greater than 4:1; using this definition, 45° and 60° pairs of jets can be defined legitimately as one-sided, which is in accordance with the view that classical doubles are twin-jet sources seen at angles of view substantially larger than 45°.

Figure 17 shows a gray-scale schlieren-type image of the pressure gradient at the head of the jet, with a plot of the flux density in a slice of the jet as contours superimposed upon it. The Mach disk is the structure perpendicular to the flow axis and is marked on the gray scale by the arrow. The peak of emission, which we would call the hot spot, is associated with the Mach disk and the material just downstream from the Mach disk. The more diffuse lobe structure

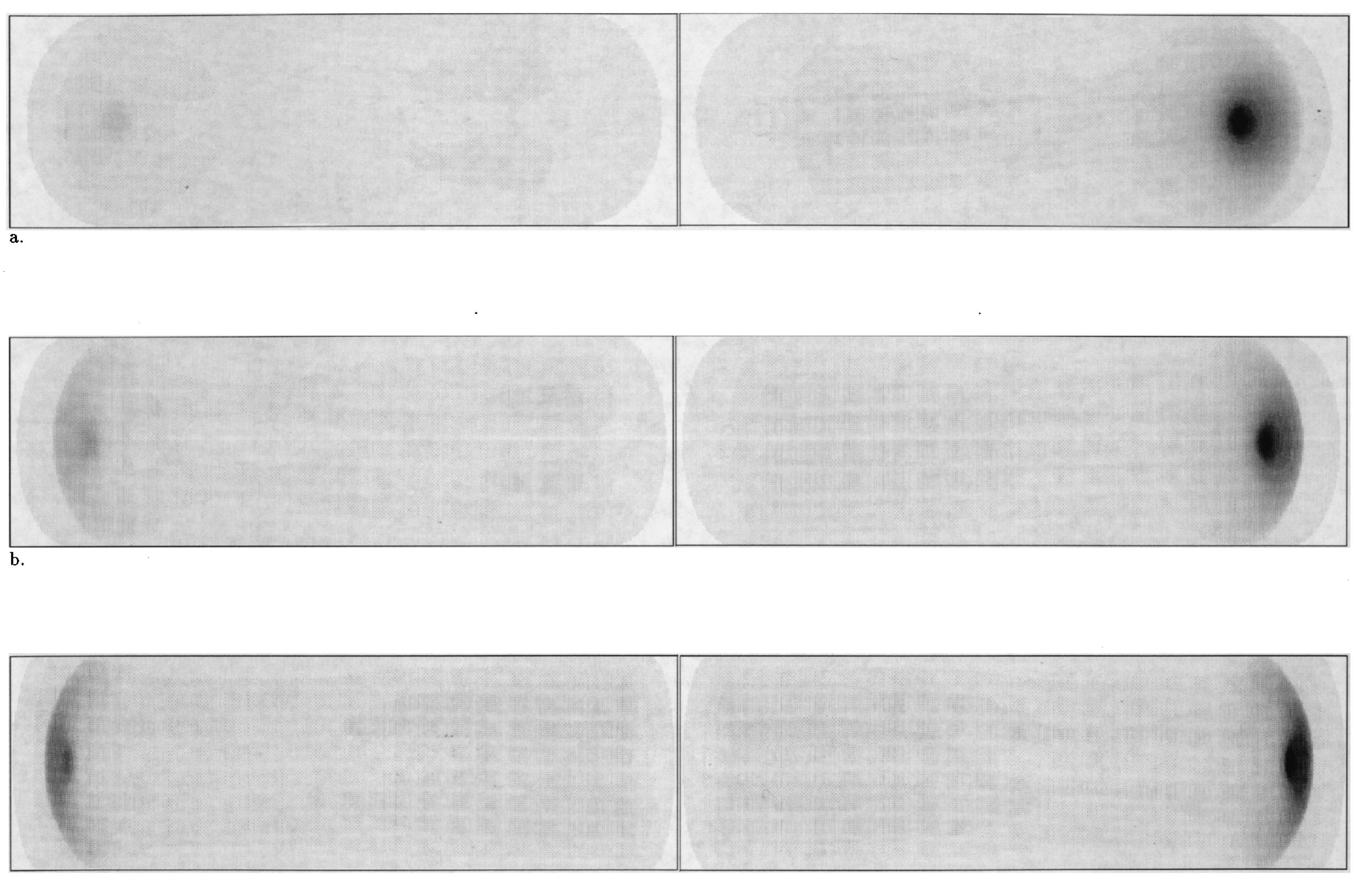

FIG. 16.—A flux density map of a two-sided jet from the simulation shown in Fig. 1*d* at viewing angles (*a*) 45°, $\mathscr{I}_{\rm max} = 5.383 \times 10^5$; (*b*) 60°, $\mathscr{I}_{\rm max} = 3.288 \times 10^5$; and (*c*) 75°, $\mathscr{I}_{\rm max} = 2.387 \times 10^5$.

FIG. 17.—Schlieren-type image of the pressure gradient at the head of the jet shown in Fig. 1*d* superimposed with white contours of the intensity at 45° of a slice through the same jet. The arrow points to the Mach disk. The contour levels are 5.0%, 6.7%, 9.1%, 12.3%, 16.6%, 22.4%, 30.2%, 40.7%, 54.9%, and 75.1% of the $\mathscr{I}_{\rm max} = 3.554 \times 10^4$.

is associated with the shocked ambient medium, just downstream from the bow shock.

We conclude that localized regions of emission near the periphery of FR II sources are likely to be associated with thermalization of the jet flow at a Mach disk and may thus be used to infer the pressure downstream of that structure, which may in turn be used to build simple analytic models for the flow dynamics (e.g., Williams 1991). The measured spectral properties of this emission are providing information on processes in shocked *jet* material, the composition of which is still debated, at points where little entrainment has occurred as the jet is cocooned for most of its length.

6. CONCLUSIONS AND FUTURE WORK

The simulated images of quiescent flows show that, for Lorentz factors in excess of ~ 5, little structure is evident within the jet. However, images of a perturbed relativistic jet seen close to the line of sight show a sequence of resolved knots along the axis similar to those seen on VLBI maps. It is striking that, although the morphology of the hydrodynamic quantities is very different from the morphology of observed jets, for small viewing angles, relativistic effects dominate, producing images that closely resemble the observations. In general, smaller viewing angles will cause bow shock structures to become less prominent in maps of parsec-scale jets because the flux density level in the knots caused by differential Doppler boosting will be much greater than the flux density level in the bow shock structures.

In the simulations using periodic perturbations, the associated light curves, whose appearance is determined by the onset of individual "events" and the overtaking of shocks by other shocks, do not reflect the periodic nature of the perturbations. In fact, it was very difficult to relate the features of a light curve to the flux density maps without a detailed examination of the hydrodynamic simulations used to make them: there is a complex relation between the maps and the underlying flow morphology. In particular, a flux density outburst associated with one of the components was the result of the interaction of two flow structures, and a detailed study of component motion revealed that apparent (slight) accelerations can be the result of a change in the spatial distribution of hydrodynamical quantities, rather than a simple acceleration of plasma or the onset of shocks.

The kiloparsec-scale jet maps suggest that the hot spot structures seen at the periphery of FR II sources are associated with internal shocks and not the bow shock. This supports the use of parameters derived for hot spots, in the construction of simple analytic models based on shock jump conditions, and the Bernoulli equation.

Work is currently in progress to admit the consideration of time delays in the radiation transfer calculations. Although we have argued here that these effects are unimportant for the studies done to date, it will be crucial to address the consequences of time delay for weak shocks that propagate at approximately the speed of the underlying flow. A modification to the hydrodynamic code is also being undertaken to include a passive magnetic field. This has major ramifications for the radiation transfer calculations, since it will permit the production of maps in the Stokes parameters Q and U, for comparison with the latest results from VLB polarimetry.

This work was supported by NSF grant AST 91-20224, and by the Ohio Supercomputer Center from a Cray Research Software Development Grant. We would like to thank T. V. Cawthorne for his helpful comments.

APPENDIX A

RELATIVISTIC EULER EQUATIONS

The hydrodynamic simulations are performed assuming axisymmetry, using as physical variables the mass density R, the momentum density M_ρ and M_z, and the total energy density E relative to the laboratory frame of reference. The gas is assumed to be inviscid and compressible with an ideal equation of state with constant adiabatic index Γ. Using cylindrical coordinates and defining the vector

$$U = (R, M_\rho, M_z, E)^T , \tag{A1}$$

the two flux density vectors

$$F^\rho = [Rv^\rho, M_\rho v^\rho + p, M_z v^\rho, (E + p)v^\rho]^T \tag{A2}$$

and

$$F^z = [Rv^z, M_\rho v^z, M_z v^z + p, (E + p)v^z]^T , \tag{A3}$$

and the source vector

$$S = (0, p/\rho, 0, 0)^T , \tag{A4}$$

the almost-conservative form of the equations is

$$\frac{\partial U}{\partial t} + \frac{1}{\rho}\frac{\partial}{\partial \rho}(\rho F^\rho) + \frac{\partial}{\partial z}(F^z) = S . \tag{A5}$$

The pressure is given by the ideal gas equation of state

$$p = (\Gamma - 1)(e - n) , \tag{A6}$$

where e and n are, respectively, the rest-frame energy density and mass density. In this work, we use units in which the speed of light, c, is unity.

The laboratory and rest-frame variables are related via a Lorentz transformation:

$$R = \gamma n , \tag{A7}$$

$$M_\rho = \gamma^2(e + p)v^\rho , \qquad M_z = \gamma^2(e + p)v^z , \tag{A8}$$

$$E = \gamma^2(e + p) - p , \tag{A9}$$

where $\gamma = (1 - v^2)^{-1/2}$ is the Lorentz factor and $v^2 = (v^\rho)^2 + (v^z)^2$.

In order to compute the pressure p and sound speed c_s, we need the rest-frame mass density n and energy density e. However, these quantities are nonlinearly coupled to the components of the velocity v^ρ and v^z, as well as to the laboratory frame variables R, M_ρ, M_z, and E via the Lorentz transformation given in equations (A7)–(A9). When the adiabatic index is constant, it is possible to reduce the computation of n, e, v^ρ, and v^z to the solution of the following quartic equation in the magnitude of the velocity v:

$$[\Gamma v(E - Mv) - M(1 - v^2)]^2 - (1 - v^2)v^2(\Gamma - 1)^2 R^2 = 0 . \tag{A10}$$

Component velocities are then given by

$$v^{\rho} = \mathrm{sign}\,(M_{\rho})v\,, \qquad v^{z} = M_{z}\,\frac{v^{\rho}}{M_{\rho}}\,. \tag{A11}$$

Then the quantities e and n can be found from the relations

$$e = E - M_{\rho}\,v^{\rho} - M_{z}\,v^{z}\,, \qquad n = \frac{R}{\gamma}\,. \tag{A12}$$

APPENDIX B

ANALYSIS OF THE TRANSITION BETWEEN EMISSIVITY AND DOPPLER BOOST DOMINATION

We wish to estimate the relative emissivity of the jet and of the post–bow-shocked ambient gas, to assess at what viewing angle the Doppler-boosted former dominates the latter, thus causing the bow shock morphology to be lost on maps with limited dynamic range. As noted in § 3, the bow shock moves forward at barely relativistic speed, thus we can use a nonrelativistic description for its pressure distribution.

In a first approximation, the jet constitutes a blunt obstacle, and the bow shock forms as a consequence of the flow over this structure, as the jet propagates into the ambient medium. At a large radial distance (r) from the axis of the obstacle, the "strength" of the bow shock, defined in terms of the velocity jump in the shock frame, falls as $r^{-3/4}$ (Landau & Lifshitz 1959). We therefore assume that

$$\frac{\Delta v}{\Delta v\,|_{\mathrm{axis}}} = \left(\frac{r_{\mathrm{jet}}}{r}\right)^{3/4}\,, \qquad r > r_{\mathrm{jet}}\,, \tag{B1}$$

the velocity (and pressure) jump being characterized by a single value in the vicinity of the Mach disk.

For a flow with adiabatic index Γ, the ratio of downstream to upstream pressures in the shock frame is

$$\frac{p_d}{p_u} = \frac{2\Gamma\mathscr{M}_u^2 - (\Gamma - 1)}{\Gamma + 1}\,, \tag{B2}$$

while the corresponding velocity ratio is

$$\frac{v_d}{v_u} = \frac{2 + (\Gamma - 1)\mathscr{M}_u^2}{(\Gamma + 1)\mathscr{M}_u^2}\,, \tag{B3}$$

where $\mathscr{M}_u$ is the upstream Mach number. Eliminating $\mathscr{M}_u$ and expressing the velocity shift as $\Delta v = v_u - v_d$,

$$\Delta v = -v_u\left[\frac{4\Gamma/(\Gamma + 1)}{(\Gamma + 1)(p_d/p_u) + (\Gamma - 1)} - \frac{2}{(\Gamma + 1)}\right]. \tag{B4}$$

On-axis, the bow shock is strong, and $p_d \gg p_u$, so that

$$\Delta v\,|_{\mathrm{axis}} \sim \frac{2v_u}{(\Gamma + 1)} = \frac{2v_{\mathrm{bow}}}{(\Gamma + 1)}\,, \tag{B5}$$

the final form arising from the fact that the bow propagates into a stationary medium.

Note that in equation (B4), v_u is $\sin\chi v_{\mathrm{bow}}$, because only that velocity component normal to the shock is modified by the shock. In general, the bow shock forms an angle χ with respect to the axis of the flow. Therefore, using equations (B1) and (B5) for the variation of Δv with r and for $\Delta v\,|_{\mathrm{axis}}$, we see that

$$\frac{p_d}{p_u} = \frac{2\Gamma/(1 + \Gamma)}{\{1 - [(r_{\mathrm{jet}}/r)^{3/4}/\sin\chi]\}} - \frac{(\Gamma - 1)}{(\Gamma + 1)}\,. \tag{B6}$$

Bow shocks appear to be approximately parabolic in form; fitting a curve of form $r^n = -a(z - z_0)$ (where z_0 is the location on the flow axis of the apex of the bow shock) to both the nonrelativistic and the extreme relativistic runs of Duncan & Hughes (1994; runs A and D) demonstrates quantitatively that $n \sim 2.2$. However, it is easily seen that using such a variation of $r(z)$ to determine χ fails if $n > 7/4$, for in that case, the pressure ratio p_d/p_u always becomes singular for some value of r. The key to this apparent problem is that, near to the apex of the bow, $\chi \sim 90°$, while for $r \gtrsim r_{\mathrm{jet}}$, the bow rapidly attains a constant angle ($\gtrsim 45°$) with respect to the axis; a parabola is a poor approximation globally. For $r \gtrsim r_{\mathrm{jet}}$, it is appropriate to take $\sin\chi$ as a constant $\mathscr{O}[1/(2)^{1/2}]$. We have checked the validity of this approximation by computing p_d/p_{stag}, with the stagnation pressure (p_{stag}) computed from $\mathscr{M}_u$ following Landau & Lifshitz; the ratio exceeds unity only for $r \lesssim r_{\mathrm{jet}}$, showing that the estimated pressure downstream of the bow shock is unphysical.

To compare the post–bow shock emission with that of the jet, we note that, as the former is essentially nonrelativistic, and thus not Doppler boosted, following the discussion of § 3, the emissivity is $\varepsilon_{\mathrm{bow}} \propto p_d^{(\alpha+3)/2}$, whereas the latter is $\varepsilon_{\mathrm{jet}} \propto p_0^{\alpha+3}\mathscr{D}^{2+\alpha}$ ($\mathscr{D}$ being the viewing angle–dependent Doppler factor). Since p_0 is the unshocked jet pressure, and the jet is taken to be initially in pressure balance with the ambient gas, p_u may be identified with p_0. The common term in p_0 (i.e., p_u) means

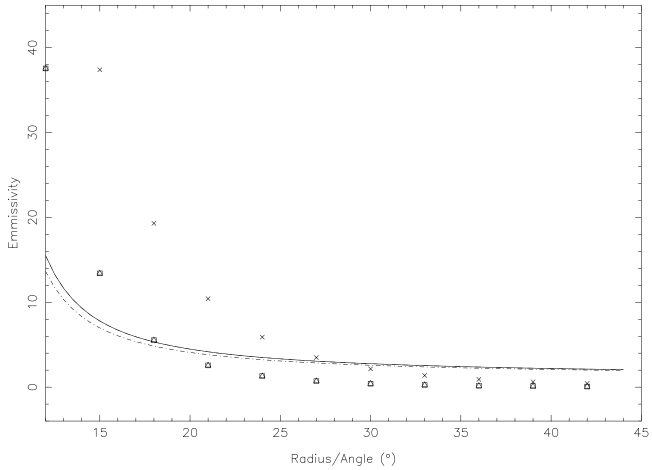

FIG. 18.—Estimate of p_d/p_u for the three relativistic runs of Duncan & Hughes as lines, and $\mathscr{D}^{2+\alpha}$ for these same runs as markers: crosses for the $\gamma = 5$ case, triangles and squares for the $\gamma = 10$ runs; χ was taken to be 55°.

that we may compare the jet and bow emissivities by comparing the values of p_d/p_u and $\mathscr{D}^{2+\alpha}$. This is done in Figure 18, which shows our estimate of p_d/p_u for the three relativistic runs of Duncan & Hughes as lines, and $\mathscr{D}^{2+\alpha}$ for these same runs as markers: crosses for the $\gamma = 5$ case, and triangles and squares for the $\gamma = 10$ runs; χ was taken to be 55°. The jet radius is six units; looking, for example, at three jet radii, we see that the Doppler boosting of the jet produces a comparable laboratory frame emissivity at an angle $\sim 18°$ for the faster flows, and at $\sim 25°$ for the slower flow. Evidently, for viewing angles $\lesssim 30°$, the Doppler-boosted jet will dominate emission from the bow more than a few jet radii off-axis.

REFERENCES

Aller, M. F., Aller, H. D., & Hughes, P. A. 1996, in ASP Conf. Ser., Blazar Continuum Variability, ed. H. R. Miller & J. R. Webb (San Francisco: ASP), in press

Aller, H. D., Aller, M. F., Latimer, G. E., & Hodge, P. E. 1985, ApJS, 59, 513

Blandford, R. D., & Königl, A. 1979, ApJ, 232, 34

Bridle, A. H., & Perley, R. A. 1984, ARA&A, 22, 319

Cawthorne, T. V. 1991, in Beams and Jets in Astrophysics, ed. P. A. Hughes (Cambridge: Cambridge Univ. Press), 187

Duncan, G. C., & Hughes, P. A. 1994, ApJ, 436, L119

Gómez, J. L., Martí, J. Mª., Marscher, A. P., Ibáñez, J. Mª., & Marcaide, J. M. 1995, ApJ, 449, L19

Einfeldt, B. 1988, SIAM J. Numer. Anal., 25, 294

Harten, A., Lax, P. D., & van Leer, B. 1983, SIAM Rev., 25, 35

Jun, B.-I., Clarke, D. A., & Norman, M. L. 1994, ApJ, 429, 748

Komissarov, S. S., & Falle, S. A. E. G. 1996, in ASP Conf. Ser. 100, Energy Transport in Radio Galaxies and Quasars, ed. P. E. Hardee, A. H. Bridle, & J. A. Zensus (San Francisco: ASP), 165

Landau, L. D., & Lifshitz, E. M. 1959, Fluid Mechanics (New York: Pergamon)

Lind, K. R., & Blandford, R. D. 1985, ApJ, 295, 358

Pacholczyk, A. G. 1970, Radio Astrophysics (San Francisco: Freeman)

Quirk, J. J. 1991, Ph.D. thesis, Cranfield Institute of Technology

Rayburn, D. R. 1977, MNRAS, 179, 603

Rybicki, G. B., & Lightman, A. P. 1979, Radiative Processes in Astrophysics (New York: Wiley Interscience)

Scargle, J. D. 1982, ApJ, 263, 835

Williams, A. G. 1991, in Beams and Jets in Astrophysics, ed. P. A. Hughes (Cambridge: Cambridge Univ. Press), 342

Williams, A. G., & Gull, S. F. 1984, Nature, 310, 33

Wilson, M. J. 1987, MNRAS, 226, 447

Wilson, M. J., & Scheuer, P. A. G. 1983, MNRAS, 205, 449

Zensus, J. A., & Pearson, T. J. 1990, Parsec-Scale Radio Jets (Cambridge: Cambridge Univ. Press)